Fiber-compatible $LiNbO_3$ Thin Film Membrane for Broadband Second Harmonic Generation

A. Zinaoui*[a], L. Grosjean[a], J.-D. Fayssaud[a], A. De Sousa Lopes Moreira[a], M. A. Suarez[a], S. Queste[a], L. Robert[a], L. Gauthier Manuel[a], M. Chauvet[a], N. Courjal[a]

[a] University Marie & Louis Pasteur, University of Franche-Comte, CNRS, FEMTO-ST institute, F-25000, France,

ABSTRACT

We introduce an original phase-matching configuration using type I birefringence phase matching (BPM), which leverages micro-waveguide dispersion and material birefringence. This approach achieves a broadband response over 150 nm in the C-telecom band with an efficiency of 40 %/W/cm². Implemented with a poling-free rib waveguide suspended on a thin film x-cut $LiNbO_3$ membrane, and combined with a titanium diffused waveguide, it minimizes injection loss to below 1 dB/facet. This structure offers greater tolerance for manufacturing uncertainties and serves as an alternative to standard thin film platforms, enabling efficient, cost-effective nonlinear photonic platforms.

Keywords: Nonlinear Optics, Lithium Niobate Thin Films, Second Harmonic Generation

1. INTRODUCTION

Broadband spectral response for frequency conversion is well demanded for applications such as broadband spectrum detection[1], high-brightness single-photon sources[2] and quantum frequency conversion[3]. The most common frequency converters in $LiNbO_3$ are based on the periodic inversion of the domain Periodic Poled Lithium Niobate (PPLN), primarily targeting high conversion efficiency, achieving 2600 %/W/cm² at telecom wavelengths[4]. This efficiency typically requires a type-0 configuration, which utilizes the highest nonlinear coefficient d_{33} = 27 pm/V of the material and a high confinement platform $LiNbO_3$ on insulator (LNOI). However, this configuration is drastically limited by a narrow spectral response around the generated wavelength, typically tens of nanometers. PPLNOI configurations must balance the trade-off between fabrication simplicity and insertion losses, with low coupling losses (< 1 dB/facet) achieved through 2D tapers requiring multiple additional fabrication steps beyond those for the waveguide[5]. Additionally, the phase-matching condition for efficient conversion becomes very stringent at interaction lengths above 5 mm, resulting in a 50-fold drop in second harmonic intensity[6-7].

Our study unveils an original phase-matching configuration based on type I birefringence phase matching (BPM), benefiting from micro-waveguide dispersion and material birefringence. The orthogonal polarization between the two interacting waves not only facilitates separation but also enables a broadband response of 150 nm at the heart of the C-telecom band, with a competitive efficiency of 40 %/W/cm². These results were achieved using a rib waveguide suspended on a thin film x-cut $LiNbO_3$ membrane. This rib waveguide is combined with a titanium diffused waveguide via an adiabatic transition, minimizing the injection loss to below 1 dB/facet and ensuring single-mode propagation between the input and output of the waveguide.

The proposed structure significantly reduces technological constraints, offering five times more tolerance compared to PPLN in height variation for an interactive length of 5 mm, thereby allowing to benefit from the overall conversion efficiency. This advancement facilitates the creation of nonlinear integrated photonic platforms, offering cost-effective manufacturing solutions.

2. MANUFACTURING PROCESS AND ITS ENERGY COST

This section details the technological process employed to fabricate a broadband frequency converter, as depicted in Figure 1. The fabrication begins with the deposition of a 6 µm wide titanium strip, which is thermally diffused at 1050 °C for 9 hours to form the Ti-indiffused waveguide. Reactive ion etching (RIE) is then applied using a 1.7 µm thick nickel mask to etch the rib waveguide with its two lateral tapers on either side of the diffused titanium structure. Subsequently, a membrane is inscribed on the back of the waveguide by dicing with a precision circular saw (3350 DISCO DAD). The SEM image in Figure 1 shows the cross-section at the bottom of two membranes side by side, with a zoom-in on the side wall framed in red. To achieve a precisely calibrated $LiNbO_3$ film thickness of around 2 µm while minimizing insertion losses, a post-thinning RIE process has been developed. This process enables further micrometer-scale thinning and precise thickness control down to 10 nm. During the saw-thinning stage, the thickness can be adjusted individually for different sections of the same wafer, providing remarkable process flexibility compared to producing wafers with uniform thicknesses.

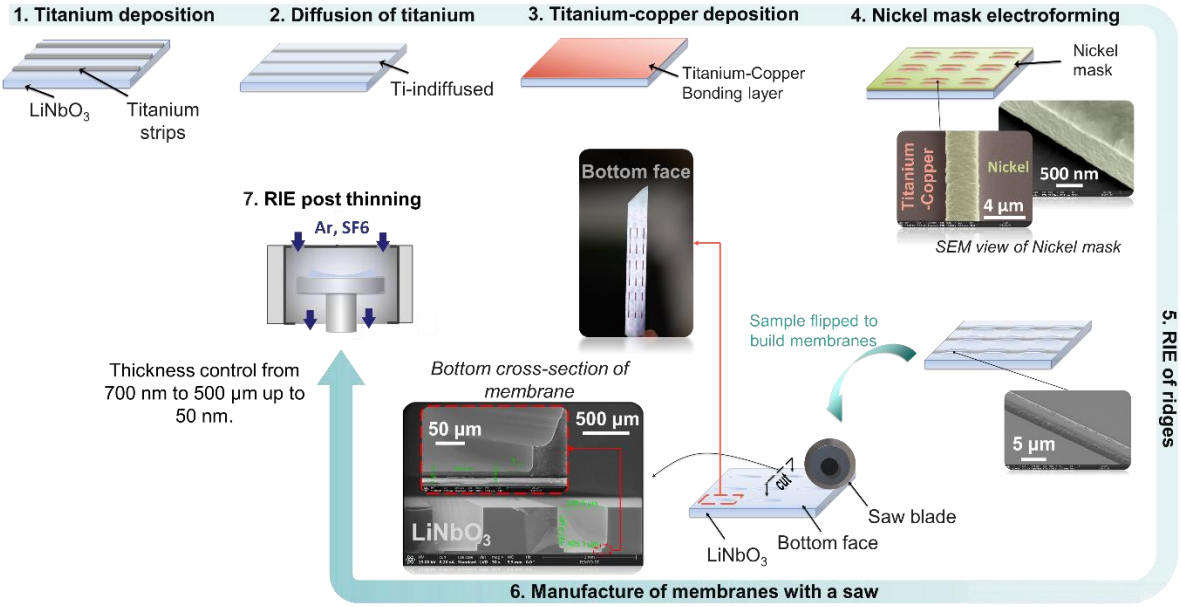

Figure 1. Schematic representation of the fabrication process for a broadband frequency converter, including titanium waveguide diffusion, rib waveguide etching, and membrane thinning.

The proposed thinning process reduces the number of fabrication steps required (eliminating bonding, ion implantation, and annealing) compared to standard LNOI processes. This simplification not only decreases technological complexity but also makes the approach easier to implement.

The energy costs of the different process steps for both LNOI and membrane technologies were assessed, as summarized in Figure 2. For the LNOI platform[8-9] (Figure 2(a)), the steps considered include helium ion implantation, SiO_2 deposition via plasma-enhanced chemical vapor deposition (PECVD), a degassing step at 450 °C for 8 hours, chemical mechanical polishing (CMP) to prepare the bonding surface, wafer bonding followed by annealing at 165 °C (16 hours), 190 °C (2 hours), and 450 °C (8 hours), a second CMP to reduce thin-film roughness, and RIE for waveguide fabrication.

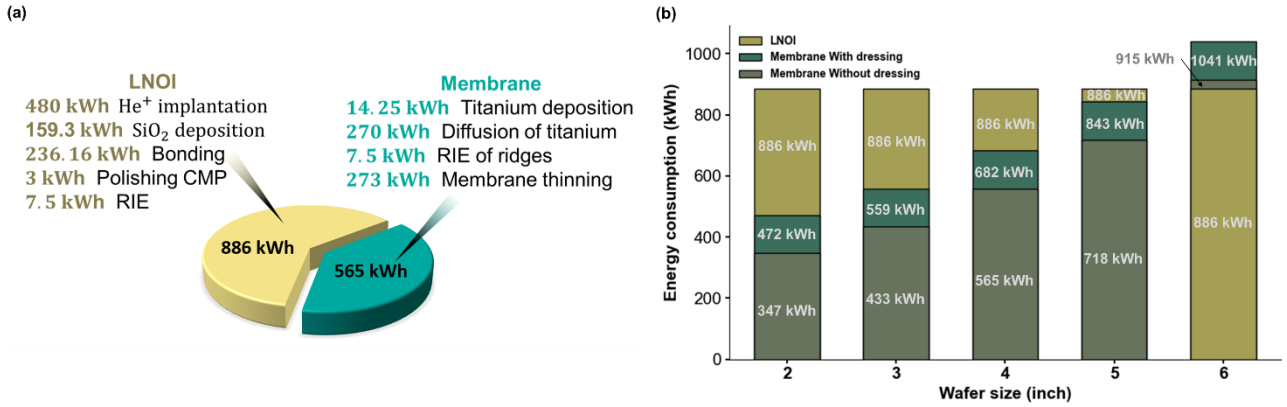

Figure 2. Comparison of energy consumption for the manufacturing processes of LNOI and membrane technologies. (a) Energy consumption for each fabrication step in LNOI technology for a 4-inch wafer scale. (b) Total manufacturing energy cost as a function of wafer size for both technologies, highlighting the scalability and energy efficiency of the membrane process for wafers under 5-inch size.

Energy consumption estimates were based on the nominal operating power of each step, multiplied by the process duration. While this approach does not fully capture real-time variations in power consumption, it provides a comparative baseline. Figure 2(b) illustrates the manufacturing energy cost per wafer size, showing that LNOI technology has an invariant energy cost per wafer, whereas membrane technology's energy cost varies with the number of membranes produced per wafer. For example, a 2-inch wafer can accommodate 50 membranes, while a 6-inch wafer can support up to 500 membranes. Each membrane offers a usable area of 4 mm², corresponding to a thin film measuring 400 µm in width and 1 cm in length, enabling the integration of multiple devices.

The membrane technology significantly reduces energy consumption, achieving an estimated energy saving of 410 kWh for a 4-inch wafer containing 150 membranes (Figure 2(a)). This efficiency highlights the energy and material advantages of the proposed approach, making it an attractive solution for broadband nonlinear photonic device manufacturing.

In terms of manufacturing energy consumption and the complexity of fabrication, membrane technology is particularly advantageous for wafer sizes smaller than 4 inches, making it ideal for small-scale mass production or on-demand device fabrication. Conversely, for high-volume production, LNOI technology becomes more appealing due to its lower energy cost per wafer for sizes exceeding 5 inches. The membrane platform provides then a flexible thin-film technology with a low energy ideal for scalable photonic applications.

3. THIN-FILM MEMBRANE-BASED SECOND HARMONIC GENERATOR

This section aims to employ membrane technology to realize a suspended rib waveguide for second harmonic generation (SHG). By exploiting the material's birefringence and the dispersion of the effective indices for ordinary and extraordinary modes, we achieve type-I phase matching between the fundamental TM_{00} pump mode and the TE_{00} second harmonic (SH) mode.

The nonlinear process takes place within the air-suspended rib waveguide located at the middle of the structure (Figure 3(a)). This rib waveguide is connected to titanium-diffused waveguides at both the input and output through tapered sections. These tapered transitions ensure smooth mode propagation into the nonlinear section, promoting single-mode operation. This design minimizes coupling losses to 0.8 dB per facet and improves light injection and collection.

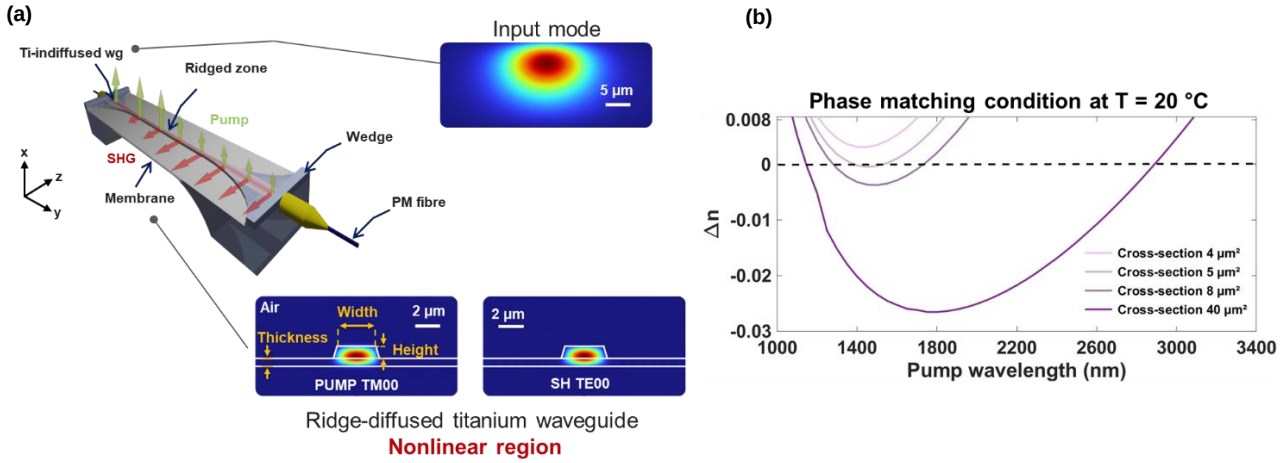

Figure 3. (a) Schematic of the air-suspended rib waveguide for second harmonic generation (SHG) and mode simulation for both pump and SH. (b) Evolution of the phase-matching condition ($\Delta n = n_{SH} - n_{Pump}$) with pump wavelength for different waveguide cross-sections.

We determine the cross-section of the rib waveguide to achieve optimal phase matching, defined by:

$$\Delta n = n_{SH} - n_{Pump} = 0 \quad (1)$$

Where n_{SHG} and n_{Pump} are the effective indices of the SHG and pump modes, respectively. Figure 3(b) shows how this phase-matching condition evolves with pump wavelength for different waveguide cross-sections. The cross-section of the waveguide is defined as width × (height + thickness), allowing a double phase matching at two different pump wavelengths separated by 500 nm for a cross-section of 8 µm², or broadband phase matching for a cross-section of 5 µm². Phase matching disappears for cross-sections below 5 µm².

The various parameters of the structure are determined using finite element analysis (FEM) with COMSOL® software. We calculate the optimal heights and widths for phase-matching and set the sidewall angle of the rib waveguide at 15°, a value derived from the RIE process, with a thickness of 500 nm. Figure 4(a) illustrates different geometric possibilities between the two curves Δn = -3e-4 and Δn = 3e-4 at the telecom wavelength of 1550 nm. Both curves allow more flexible phase matching corresponding to an interaction length of 1 mm. If we tolerate more than half of the maximum SHG response, the condition in Equation 1 becomes more flexible:

$$\Delta n < \frac{0.4429\,\lambda_{Pump}}{2L} \quad (2)$$

where L is the rib waveguide length. This condition depends on the interaction length between the pump and the SH. For a length L = 5 mm, the phase-matching condition becomes more stringent, which reduces the fabrication tolerance (Figure 4(b): the tolerance is 10 nm in height and 25 nm in width). However, this tolerance is still 5 times higher than $LiNbO_3$ nano-waveguides[7].

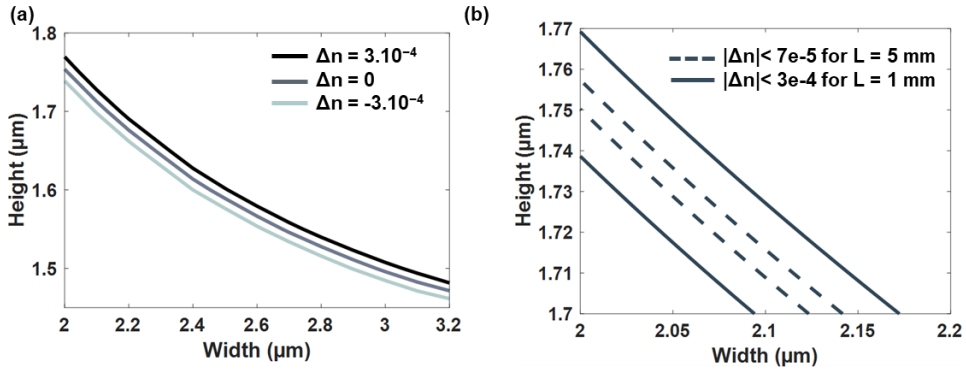

Figure 4. (a) Geometrical possibilities for the suspended rib waveguide at a fixed thickness of 500 nm and sidewall angle of 15 °. The simulation was performed at the pump wavelength of 1550 nm and a temperature of 20 °C. (b) Evolution of the fabrication tolerance for the phase-matching condition as a function of waveguide interaction length. For a 5 mm interaction length, the condition becomes more stringent, with tolerances of 10 nm in height and 25 nm in width.

The key feature of type-I phase matching is its temperature dependence, a consequence of the temperature dependence of the extraordinary index. Temperature thus adjusts both the pump and SH wavelengths. To investigate this, we simulated the conversion efficiency as a function of both the pump wavelength and temperature for an 8µm² cross-section: width = 3.8 µm, height = 1.2 µm and thickness = 800 nm. The conversion efficiency[10] is given by:

$$\eta_{\text{norm}} = \frac{P_{\text{SHG}}}{P_{\text{pump}}^2 L^2} = \frac{8\pi^2}{\varepsilon_0 c n_{\text{pump}}^2 n_{\text{SHG}} \lambda_{\text{pump}}^2} \frac{\xi^2 d_{\text{eff}}^2}{A_{\text{eff}}} \tag{3}$$

Where P_{SHG} and P_{Pump} is the respective SHG and pump intensity, c is the speed of light in vacuum, ε_0 is the dielectric permittivity of vacuum, d_{eff} is the nonlinear effective coefficient of order 2 equal to 4.3 pm/V, A_{eff} is the effective mode area and ξ is the spatial overlap integral of the two modes.

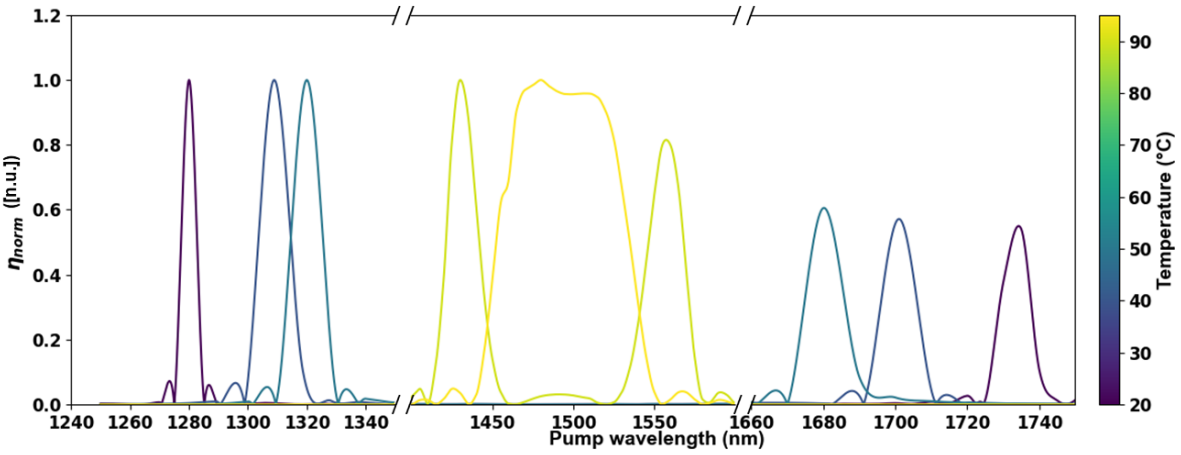

Figure 5. Conversion efficiency simulation as a function of pump wavelength and temperature for an 8 µm² cross-section waveguide. The conversion efficiency is shown for a temperature variation of 75°C, with a wide tunability band from 1280 nm to 1740 nm.

This design provides a tunability band of nearly 500 nm, from 1280 nm to 1740 nm, producing visible wavelengths between 640 nm and 870 nm over a temperature range of 75°C (Figure 5). To achieve an even wider tuning range, the

waveguide cross-section must be increased. For example, a waveguide cross-section of 23 µm² offers a tunability band of approximately 1000 nm over a temperature range of 180°C, generating multiple wavelengths from green to red in the visible range with a single waveguide. The conversion efficiency remains competitive at 50%/W/cm² at a wavelength of 1550 nm, thanks to the 98 % modal overlap between the two interacting waves and the reduced waveguide cross-section.

After fabricating the 8 µm² cross-section structure with a 1 mm interaction length, we used the experimental setup shown in Figure 6(a) to characterize the nonlinear response. The sample is mounted on a temperature-controlled oven. A Polarization Maintaining (PM) fiber is used at the waveguide input to excite the TM_{00} pump mode, and it is connected to a tunable laser in the 1350 to 1650 nm range. The output beams are collected using a microscope objective and detected with a silicon detector for the second harmonic and a germanium detector for the pump beam.

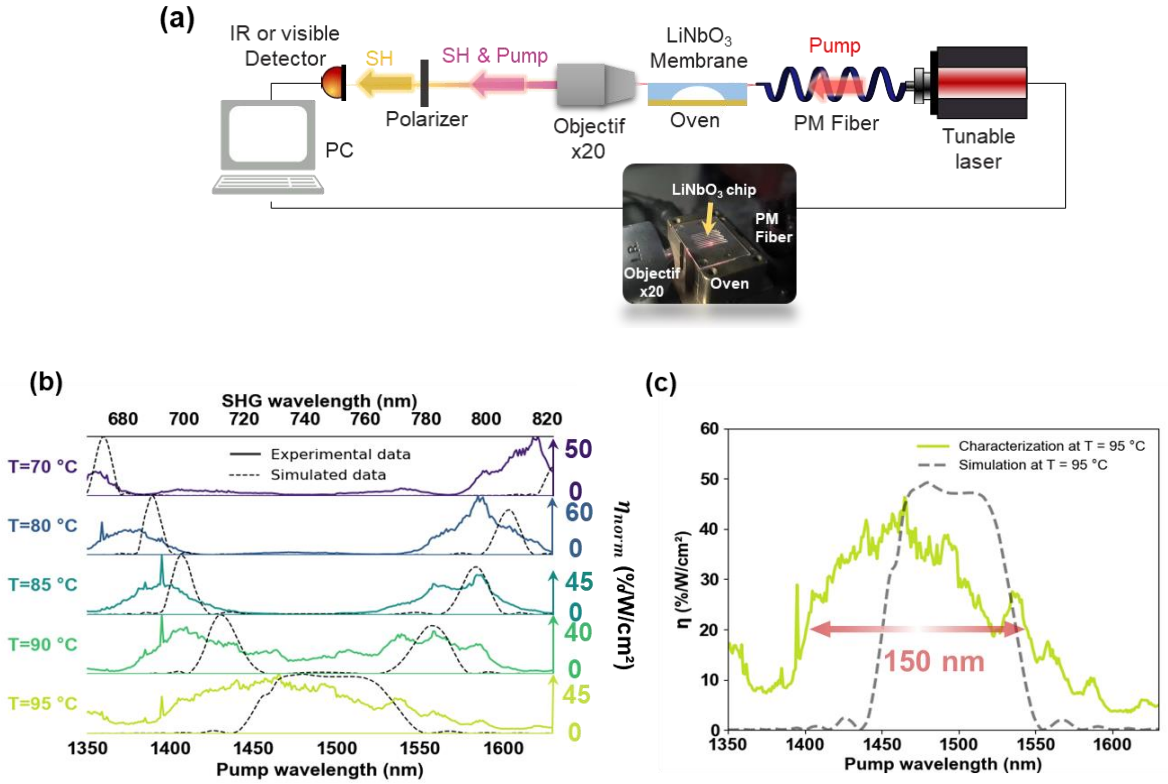

Figure 6. (a) Experimental setup for characterizing the nonlinear response of the suspended rib waveguide. (b) Experimental nonlinear conversion response with an evolution of the conversion efficiency as a function of temperature. A dual-phase matching within the telecom band is demonstrated, resulting in a broadband response of 150 nm. (c) 150 nm broadband response at 95 °C with a conversion efficiency of 40%/W/cm².

Since the two interacting waves have orthogonal polarization, their collection at the output is facilitated. By measuring the corresponding powers, we can determine the conversion efficiency (Eq. 3). Figure 6(b) shows the evolution of conversion efficiency as a function of temperature. We demonstrated double-phase matching that spans the telecom band and merges into the band centered at 1480 nm, resulting in a broadband response of 150 nm (Figure 6(c)). With available laser sources, we demonstrated a tunability band of 300 nm, from 1350 nm to 1650 nm, for a temperature variation of 70 °C to 95 °C. Theoretically, we showed that a tunability band of 460 nm, from 1280 nm to 1740 nm, could be achieved with the same waveguide cross-section. The significant thermal tunability of the waveguide is a key feature of type-I SHG, allowing coverage of two critical telecom wavelength windows, from 1.3 to 1.7 µm, with a single component. Thanks to the small waveguide cross-section and modal overlap between the pump and SH, the conversion efficiency remains competitive at approximately 40 %/W/cm².

4. CONCLUSION

In conclusion, the thin-film membrane-based second harmonic generation platform combines cost-effectiveness and accessibility to achieve exceptional thermal tunability from 1.3 μm to 1.7 μm, significantly exceeding commercial products by an order of magnitude. This is accomplished while maintaining a competitive conversion efficiency of 40 %/W/cm². The larger cross-section of the rib waveguide, compared to nano-waveguides, relaxes fabrication constraints, enabling the development of centimeter-long nonlinear devices and boosting the overall efficiency to nearly 100 % with pump powers of approximately 100 mW. This innovation paves the way for a new generation of compact, broadband, and energy-efficient nonlinear thin-film technologies.

5. ACKNOWLEDGEMENT

This work has been partially funded by the SYRAH-lab project (Contract No. ANR-19- LCV2-0007-01), the NanoFiLN project (Grant No. ANR-23-PEEL-0004), the EIPHI Graduate school (Contract No. ANR-17-EURE-0002), and the French RENATECH network through its FEMTO-ST technological facility

REFERENCES

[1] A. Y. Hwang, H. S. Stokowski, T. Park, M. Jankowski, T. P. McKenna, C. Langrock, J. Mishra, V. Ansari, M. M. Fejer, and A. H. Safavi-Naeini, "Mid-infrared spectroscopy with a broadly tunable thin-film lithium niobate optical parametric oscillator," Optica 10, 1535 (2023). DOI: https://doi.org/10.1364/OPTICA.502487

[2] Z. Ma, J.-Y. Chen, Z. Li, C. Tang, Y. M. Sua, H. Fan, and Y.-P. Huang, "Ultrabright quantum photon sources on chip," Phys. Rev. Lett. 125, 263602 (2020). DOI: https://doi.org/10.1103/PhysRevLett.125.263602

[3] X. Wang, X. Jiao, B. Wang, Y. Liu, X.-P. Xie, M.-Y. Zheng, Q. Zhang, and J.-W. Pan, "Quantum frequency conversion and single-photon detection with lithium niobate nanophotonic chips," npj Quantum Inf. 9, 38 (2023). DOI: https://doi.org/10.1038/s41534-023-00704-w

[4] C. Wang, C. Langrock, A. Marandi, M. Jankowski, M. Zhang, B. Desiatov, M. M. Fejer, and M. Loncar, "Ultrahigh efficiency wavelength conversion in nanophotonic periodically poled lithium niobate waveguides," Optica 5, 1438 (2018). DOI: https://doi.org/10.1364/OPTICA.5.001438

[5] Changran Hu, An Pan, Tingan Li, Xuanhao Wang, Yuheng Liu, Shiqi Tao, Cheng Zeng, and Jinsong Xia, "High-efficient coupler for thin-film lithium niobate waveguide devices," Opt. Express **29**, 5397-5406 (2021). DOI: https://doi.org/10.1364/OE.416492

[6] P.-K. Chen, I. Briggs, C. Cui, L. Zhang, M. Shah, and L. Fan, "Adapted poling to break the nonlinear efficiency limit in nanophotonic lithium niobate waveguides," Nat. Nanotechnol. 19, 44–50 (2024). DOI: https://doi.org/10.1038/s41565-023-01525-w

[7] P. S. Kuo, "Noncritical phasematching behavior in thin-film lithium niobate frequency converters," Opt. Lett. 47, 54 (2022). DOI: https://doi.org/10.1364/OL.444846

[8] Yuechen Jia, Lei Wang, Feng Chen, "Ion-cut lithium niobate on insulator technology: Recent advances and perspectives". *Appl. Phys. Rev.* 1 March 2021; 8 (1): 011307. DOI: https://doi.org/10.1063/5.0037771

[9] Poberaj, G., Hu, H., Sohler, W. and Günter, P, "Lithium niobate on insulator (LNOI) for micro-photonic devices". Laser & Photon. Rev., 6: 488-503 (2012). DOI: https://doi.org/10.1002/lpor.201100035

[10] R. Luo, Y. He, H. Liang, M. Li, and Q. Lin, "Highly tunable efficient second-harmonic generation in a lithium niobate nanophotonic waveguide," Optica 5, 1006 (2018). DOI: https://doi.org/10.1364/OPTICA.5.001006